A CCD Spectroradiometer for Ultraviolet Actinic Radiation Measurements

EVELYN JÄKEL* AND MANFRED WENDISCH*

Leibniz-Institute for Tropospheric Research (IfT), Leipzig, Germany

MARIO BLUMTHALER

Innsbruck Medical University, Innsbruck, Austria

RAINER SCHMITT

Meteorologie Consult GmbH (metcon), Königstein, Germany

ANN R. WEBB

University of Manchester, Manchester, United Kingdom

(Manuscript received 20 December 2005, in final form 23 June 2006)

ABSTRACT

A new spectroradiometer for spectral measurements of ultraviolet (UV) atmospheric radiation (290–400 nm) using a charge coupled device (CCD) as a detector is introduced. The instrument development is motivated by the need for measurements with (a) high accuracy in the UV-B spectral range (290–315 nm) for photochemistry applications and (b) high temporal resolution in quickly changing atmospheric conditions such as partial cloud cover. The new CCD instrument is mainly intended for airborne use. It allows fast data collection (<300 ms time resolution for each spectrum) with improved sensitivity in the UV spectral range. The instrumental setup and its characterization in terms of stray light, dark current, noise, and detection limits are described and compared to a spectroradiometer with a photodiode array (PDA) detector. The new CCD spectroradiometer has a one order of magnitude greater sensitivity than the PDA-based spectroradiometer. However, the stray light of the CCD instrument is wavelength dependent, which requires a more complicated data evaluation procedure than the PDA instrument. Comparison with other UV spectroradiometers (a PDA spectroradiometer and two ground-based double monochromators) shows the advantages of the CCD system for UV-B measurements of actinic flux densities and photolysis frequencies of ozone and nitrogen dioxide, and the improved performance compared to PDA spectroradiometers.

1. Introduction

Accurate atmospheric measurements of spectral ultraviolet (UV) radiation (290–400 nm) are challenging, in particular, in spatially inhomogeneous atmospheric and surface albedo conditions. The absorption of UV radiation due to the stratospheric ozone causes a strong decrease of the downward UV reaching the troposphere. It causes a sudden drop of the spectral radiation of several orders of magnitudes toward smaller wavelengths (λ), which is referred to as the atmospheric cutoff. The short wavelength limit of this cutoff depends on the vertical total ozone column (TOC) and the solar zenith angle (SZA). It usually ranges between 290- and 320-nm wavelength at the ground. Highly sensitive spectroradiometers are required to detect the remaining small amount of UV radiation reaching the lower troposphere. However, the UV portion of solar radiation is important with regard to biological and photochemical processes. Ultraviolet radiation affects humans (skin, eyes, immune system) and other elements

* Current affiliation: Institute for Atmospheric Physics, University of Mainz, Mainz, Germany.

Corresponding author address: Evelyn Jäkel, Institute for Atmospheric Physics, University of Mainz, Becherweg 21, 55099 Mainz, Germany.
E-mail: jaekel@uni-mainz.de

DOI: 10.1175/JTECH1979.1

of the biosphere (animals, plants, and aquatic ecosystems) (van den Leun et al. 1998). To quantify these effects the solar UV irradiance F is introduced, where F (in units of W m^{-2} nm^{-1}) comprises the radiation energy flux incident onto a flat *unit surface*. In contrast to F, the spectral actinic flux density F_a (in units of W m^{-2} nm^{-1}) is defined as a spherical flux density, integrating the radiation incident from all directions onto the surface of a *unit sphere* (Madronich 1987):

$$F_a(\lambda) = \int_0^{2\pi} \int_{-1}^{1} L(\theta, \Phi, \lambda)\sin\theta \, d\theta \, d\Phi, \qquad (1)$$

with L being the spectral radiance (in units of W m^{-2} nm^{-1} sr^{-1}), θ the incident angle of the radiation (in °), and Φ the azimuth angle (in °). In this way F_a quantifies the radiation energy available for photochemical processes.

Atmospheric chemistry processes are dependent on the photolysis of trace gases resulting in the production of reactive radicals. The hydroxyl radical (OH) is one of the most prominent radicals in the earth's atmosphere (Ehhalt 1999; Heard and Pilling 2003; Monks 2005) and is primarily produced by the photolysis of ozone. The photolysis frequency J, which constitutes the first-order rate coefficient of a photochemical dissociation process, depends on the available F_a, the absorption cross-section σ of the parent molecules, and the quantum yield ϕ of the photoproducts, both being functions of wavelength:

$$J = \int \sigma(\lambda)\phi(\lambda)F_a(\lambda) \, d\lambda \, . \qquad (2)$$

Spectroradiometers make possible the calculation of J values for any gas species whose absorption cross section and quantum yield are known and exhibit significant values within the measured wavelength range. Quantifying and understanding of atmospheric photochemical processes require airborne and ground-based measurements of spectral actinic flux densities F_a. In this work the photolysis frequencies of ozone [$O_3 + h\nu \rightarrow O(^1D) + O_2$] and nitrogen dioxide ($NO_2 + h\nu \rightarrow NO + O$) are considered in particular, the former being the primary source of OH and the latter the major route for tropospheric ozone formation.

Spectroradiometers measure F or F_a depending on the angular response of the optical inlet (collector), which collects the radiation photons. Whereas irradiance measurements require a cosine-angular weighting of the photons by the optical inlet, the actinic radiation is measured using isotropic (i.e., incident-angle independent) optical inlets. The collected radiation is transmitted via fiber optics to a spectrometer, where the radiation is quickly dispersed into its component wavelengths using monochromators (single or double gratings) and then detected as a function of wavelength. Scanning single or double monochromators direct the radiation at a time onto the detector by moving the diffraction grating(s), whereas fixed gratings image the entire spectrum on the detector (PDA or CCD). So far photomultiplier tubes (PMTs) or photodiode arrays (PDAs) have been used as detectors. In this paper a new spectroradiometer type is described that uses a charge coupled device (CCD) as a detector.

The first actinic flux density measurements using a scanning double-monochromator system with a PMT detector were described by Hofzumahaus et al. (1999) for ground-based applications and by Shetter and Müller (1999) for airborne data collection. Both scanning spectroradiometers recorded the actinic flux density in the spectral range between 280 and 420 nm with a wavelength resolution of 1 nm. Depending on the spectral resolution, the minimum time resolution needed to scan an entire spectrum was between 10 and 90 s (Lefer et al. 2001). The time-consuming wavelength scanning may lead to a distortion of the spectrum, in particular for inhomogeneous cloud or surface albedo conditions. This problem has to be considered for both ground-based applications and is even more problematic for airborne measurements. In practice spectroradiometers do not completely isolate a particular spectral component from all other wavelengths but they do transmit residual radiation from "out of band" wavelengths. This issue is known as the stray light problem; removing the out-of-band radiation is called stray light rejection. The main advantage of using a double monochromator is its excellent ability to remove the stray light, which is crucial for accurate actinic flux density and irradiance measurements in the UV-B spectral range ($\lambda < 315$ nm). The disadvantages of the wavelength-scanning systems are the poor time resolution (in the range of minutes) and a limited wavelength stability. The wavelength stability of double-monochromator spectroradiometers is limited by the unavoidable mechanical movements of the gratings during the wavelength-scanning process. For airborne operation, in particular with possible turbulent aircraft movements, the mechanical stability of the scanning mechanics is not always guaranteed.

In recent years single monochromators (also called multichannel spectrometers, MCSs) with a PDA detector have been increasingly applied for airborne and ground-based measurements of actinic flux density and irradiance (Wendisch et al. 2001; Edwards and Monks 2003; Pilewskie et al. 2003; Wendisch et al. 2004; Jäkel et al. 2005; Wendisch et al. 2005). The main benefit of

a PDA detector is a high time resolution (less than 1 s) and the mechanical stability by using a fixed grating (Jäkel et al. 2005). The disadvantages of a single monochromator with a PDA detector are the poor stray light rejection and a decreased sensitivity compared to a double-monochromator spectroradiometer with a PMT detector. Hence, precise measurements of UV-B radiation are restricted to wavelengths larger than ~300 nm, depending on the intensity of the solar radiation. For large solar zenith angles and large total ozone columns the lowest reliable wavelength of the PDA detector spectroradiometer is shifted to large wavelengths.

Such a PDA spectroradiometer system was first designed and applied for airborne measurements of actinic flux densities by Jäkel et al. (2005) and Jäkel et al. (2006). This instrument was called actinic flux density meter (AFDM-PDA). The AFDM-PDA measures downwelling and upwelling spectral F_a separately using two PDA-based spectroradiometers, each connected with an optical inlet that is mounted at the top and bottom of the aircraft. The reliable spectral range of the AFDM-PDA is between 305 and 700 nm (Jäkel et al. 2005). For the photolysis frequency of ozone, deduced from the respective actinic flux density measurements [see Eq. (2)], a parameterization method was developed that extrapolates the missing $F_a(\lambda)$ data below the lower threshold wavelength (305 nm) of the AFDM-PDA (Jäkel et al. 2006). However, UV-B actinic flux densities cannot be measured with sufficient accuracy by the AFDM-PDA. Therefore, the PDA spectroradiometer was replaced by a CCD spectroradiometer with a higher sensitivity in the UV-B spectral range. This new AFDM-CCD is introduced in this paper.

A detailed description, including characterizations of the stray light behavior, signal-to-noise ratio, and detection limit of the AFDM-CCD is given in section 2, followed by examples of ground-based measurements taken during an intercomparison with double monochromators and a PDA spectroradiometer in section 3. In section 4 a short summary of the paper is given.

2. Instrumental

a. Setup

The AFDM-CCD consists of components manufactured by different companies. The final assembly was fabricated by Meteorologie Consult GmbH (metcon, Königstein, Germany). A general overview of the setup of the AFDM-CCD is presented in Fig. 1. The main components are the optical inlet (manufactured by metcon), the optical fibers (distributed by Prinz Optics GmbH, Stromberg, Germany), a housing including an MCS and a preamplifier (manufactured by Zeiss GmbH, Jena, Germany), and a housing with cooling electronics and front end electronics (FEE, manufactured by tec5, Oberursel, Germany). The FEE controls the signal generation of the CCD (manufactured by Hamamatsu Photonics, K.K., Hamamatsu City, Japan) and digitizes the analog video signal (manufactured by tec5, Oberursel, Germany). For data acquisition (DAQ) a personal computer (PC) is used with a PC interface card (manufactured by tec5). These interface electronics control the FEE and generate the integration time. Typical scan times are between 50 and 300 ms depending on the atmospheric radiation level. The enlargement in Fig. 1 shows the MCS, which is mounted in a ceramic body. The UV-enhanced optical fiber is connected to the spectrometer by a standard mechanical adapter (SMA). The radiation passes through an entrance slit (20 μm) and is dispersed by a flat-field diffraction grating (248 lines per mm), which is blazed (optimized efficiency degree) at a wavelength of 250 nm. In addition to its dispersive function, the grating images the entrance slit on the CCD detector. The CCD is thermoelectrically cooled by an integrated Peltier element to reduce the noise and to improve the temporal stability of the offset. The technical specifications of the AFDM-CCD are listed in Table 1.

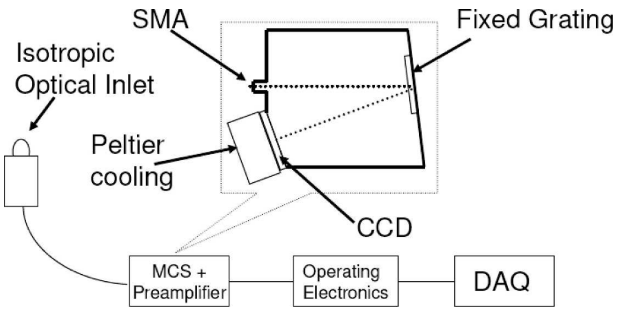

FIG. 1. Schema of the AFDM-CCD: CCD, charge coupled device; DAQ, data acquisition; MCS, multichannel spectrometer; and SMA, standard mechanical adapter.

The main difference of the AFDM-PDA setup compared to the AFDM-CCD is the detector type. Instead of a two-dimensional CCD (used in the new AFDM-CCD), a one-dimensional noncooled photodiode array (manufactured by Hamamatsu Photonics, K.K., Hamamatsu City, Japan) with 512 pixels is used in the AFDM-PDA for detection of actinic radiation within the wavelength range 280–700 nm. The grating of the AFDM-PDA is blazed at 450 nm. Overall, the AFDM-PDA is optimized for measurements in the visible spectral range. The entrance slit width is 70 μm. Due to the lower sensitivity of the PDA compared to the CCD in the UV-B, the typical scan times are higher (300–1000

TABLE 1. Instrumental specifications of the AFDM-CCD and AFDM-PDA.

Parameter	AFDM-CCD	AFDM-PDA
Input optics	2π sr quartz diffuser	
Optical fibers	Monofibers with 600-μm diameter	
Grating (lines per mm)	248	
Flat field blazed at (nm)	250	450
Wavelength range (nm)	260–680	280–700
Wavelength resolution (nm)	0.8	0.8
Bandpass (FWHM, in nm)	1.5	2.6
Detector	CCD	PDA
No. of pixels	532 × 64	512
SNR	650:1 (50 ms), 450:1 (300 ms)	140:1 (50 ms), 1700:1 (300 ms)
Typical scan times (ms)	50–300	200–1000

ms). More detailed information is given in Table 1 and by Jäkel et al. (2005).

b. CCD versus PDA spectroradiometer

To investigate the performance of the AFDM-CCD to measure UV-B radiation and to compare with the AFDM-PDA, the following parameters are considered: 1) the signal offset components including the dark current, electronic offset, and stray light contribution; 2) the sensitivity of the spectroradiometer; 3) the signal-to-noise ratio (SNR) and detection limit; and 4) the spectral resolution (wavelength steps) and the full width at half maximum (FWHM).

1) SIGNAL OFFSET COMPONENTS

The overall signal offset consists of the dark current signal plus an electronic offset and a stray light contribution. The dark current arises from thermally generated electrons in the CCD and depends mainly on the instrument's temperature. In contrast to the electronic offset, the stray light and dark current depend on the integration time. Stray light signals include undesired signals originating from other wavelengths or from misguided radiation within the instrument caused by. For example, reflections on the spectrometer walls.

(i) Dark current and electronic offset

The sum of the dark current and electronic offset can be measured when the optical inlet is completely obscured. Both can be distinguished by their different dependences on the integration time. The electronic offset is independent of the integration time whereas the dark current is integration time dependent. In the following, measurements with the obscured inlet are called "d + e measurements" and the respective signals

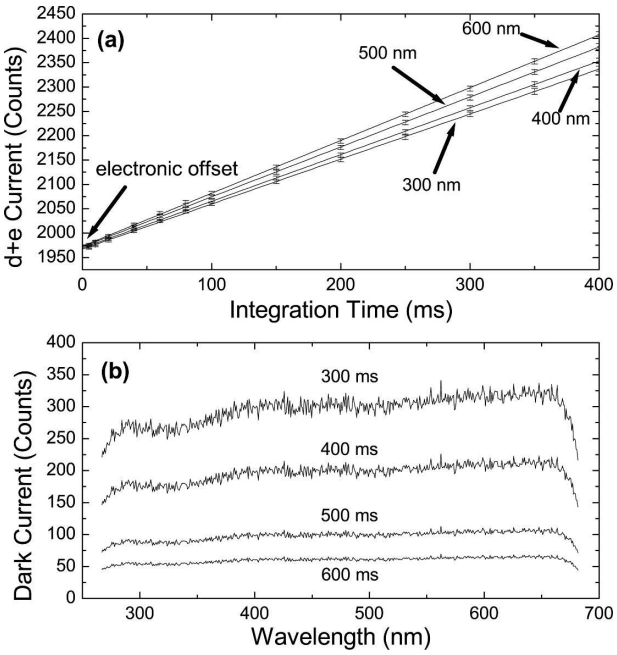

FIG. 2. Integration time dependence of the (a) d + e and (b) dark currents plotted as a function of wavelength. The error bars in (a) indicate the standard deviation of the averaged spectra (average of 1000 single spectra). The dark current as a function of wavelength in (b) is plotted for four integration times (60, 100, 200, and 300 ms).

are called the "d + e current." The number of thermally generated electrons is subject to randomized variations, which influence the d + e current. Therefore, it is advisable to consider a mean of several d + e measurements. The integration time dependence of the d + e current is shown for different wavelengths (300, 400, 500, and 600 nm) in Fig. 2a. The linear regressions of the d + e current (given as follows: d + e current = integration time × dark current + electronic offset) are used to determine the electronic offset (arrow in Fig. 2a). The spectral electronic offset corresponds to the extrapolated value of the linear regression lines at an integration time of 0 ms. A wavelength-averaged value of the electronic offset of 1970 counts with a standard deviation of 3 counts was calculated, which means that a spectral variability of the electronic offset of less than 0.2%. After subtracting the electronic offset from the d + e current, a dark current remains that is wavelength dependent and that shows a certain pixel-to-pixel variation (see Fig. 2b). The spectral variability of the dark current (standard deviation averaged over wavelength ≈7%) is higher than that of the electronic offset. To determine the spectral variability of the overall offset, the sum of the electronic offset and the dark current is crucial. In this case a spectral variability of 3% was calculated for the wavelength-averaged d + e current

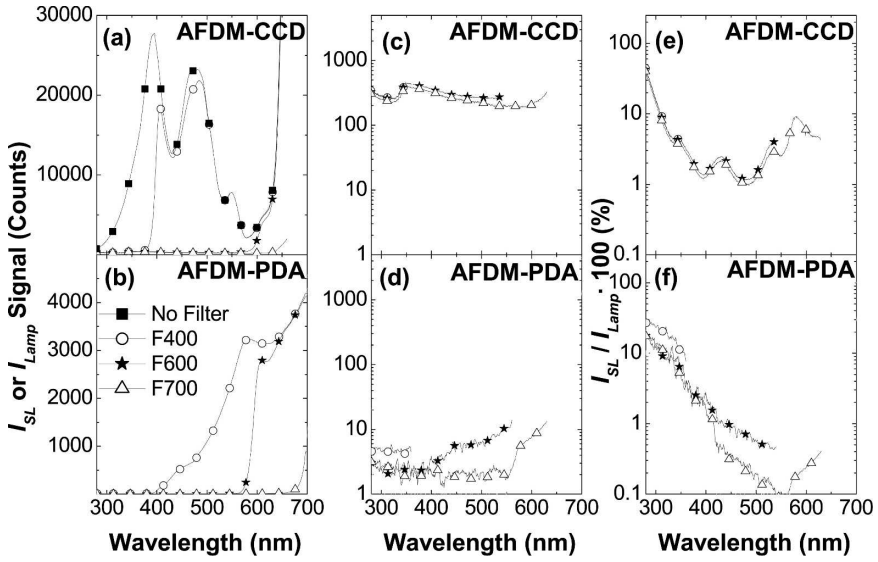

FIG. 3. Laboratory measurements of wavelength-dependent stray light counts I_{SL} of the (a) AFDM-CCD and (b) AFDM-PDA using longwave pass filter with λ_c = 400 (F400), 600 (F600), and 700 nm (F700). (c), (d) Logarithmic plots of the stray light counts I_{SL} for both spectroradiometers derived from filter measurements. Additionally, the spectral counts without using a longwave pass filter (minus I_{d+e}), I_{Lamp}, are plotted as solid lines with full squares. (e), (f) Percentage of stray light relative to the lamp spectrum.

measured for an integration time of 1000 ms. For comparison, for the AFDM-PDA the standard deviation of the d + e current for the same integration time was less than 1% (Jäkel et al. 2005). In contrast to the AFDM-PDA, the wavelength dependence of the dark current signal of the AFDM-CCD is not negligible. Consequently, the d + e offset of the AFDM-CCD must be considered in a different way compared to the AFDM-PDA.

There are two ways to deal with the wavelength dependence of the AFDM-CCD d + e measurement offset. The first one requires spectral d + e measurements for each integration time, which are then subtracted from the measured spectra. The second possibility uses a 100-ms dark current multiplied by the integration time ratio. Finally, the sum of the revised dark current and the electronic offset is subtracted from the measured spectra. During the field measurements the first method was applied. The d + e measurements were performed before and after each flight for different integration times. A deviation of the d + e currents (for each integration time) in the range of less than 1% was observed during a 4-week campaign. This results in an uncertainty for F_a of ±5%, when the d + e offset is shifted within the range of 1%.

(ii) Stray light

Spectral filters are used for stray light measurements. These filters block certain wavelength regions. Spectral radiation that is measured out of the blocked wavelength range is considered as the stray light contribution (after subtraction of the d + e current). Stray light measurements were performed in the laboratory [using a 1000-W standard tungsten irradiance lamp, traceable to the Physikalisch Technische Bundesanstalt (PTB)] and in atmospheric conditions (using the sun as the radiation source). Atmospheric measurements of the stray light contribution have the advantage that the spectral pattern of the stray light is measured in real conditions. On the other hand, laboratory measurements provide more constant and controlled circumstances. The stray light of the two spectroradiometers was quantified using spectral cutoff filters (manufactured by LOT Oriel, Darmstadt, Germany). Visible (VIS) longwave pass filters (cutting wavelengths λ_c: 400, 600, and 700 nm) have been employed. Here, λ_c is defined as the wavelength where the spectral filter transmission is 50%. A rejection of radiation of ≤99% is reached at $0.9\lambda_c$. If the spectroradiometer measures a signal that differs from the d + e current below $0.9\lambda_c$, then the difference between the measured counts I_{Filter} and the d + e current I_{d+e} using a longwave pass filter with λ_c is defined as the stray light signal:

$$I_{SL}(\lambda) = I_{Filter}(\lambda) - I_{d+e}(\lambda). \quad (3)$$

Figures 3a, 3c, and 3e show the spectral stray light signals I_{SL} for the AFDM-CCD derived from the laboratory experiments using different longwave pass filters.

For comparison, results for the AFDM-PDA are depicted in Figs. 3b, 3d, and 3f, respectively. Additionally, the counts (minus I_{d+e}) of the lamp spectrum measurement (with no filter) are displayed (I_{Lamp}). The different sensitivities of the AFDM-PDA and the AFDM-CCD cause significantly different spectral courses of the filtered and nonfiltered measurements (Figs. 3a and 3b) even though the same lamp was used. Figures 3c and 3d display the stray light counts I_{SL} in a limited wavelength range (280–450 nm) on a logarithmic scale. Note that the curves in Figs. 3c–f are plotted up to a wavelength that corresponds with the filter cutting wavelength $0.9\lambda_c$. It is shown that the level of stray light counts below the cutoff wavelength of the filter depends on the filter that is used for the following reasons. (a) The measured signal using a filter results in a generally lower signal due to the transmission of the filter (not identical to one) even in the spectral range larger than the cutting wavelength. (b) The broader the filter range is, the more the signal decreases. It is quite evident that lower signals cause lower stray light. However, the spectral shape of the stray light contribution can be studied from this type of figure. In contrast to the AFDM-PDA, the AFDM-CCD shows a distinct wavelength dependence of the stray light counts I_{SL} with a maximum around 340–350 nm. The influence of the stray light contribution on F_a and J values is discussed in section 3.

In Figs. 3d and 3e the stray light counts I_{SL} are scaled to the lamp spectrum. Here, I_{SL} influences the total signal mainly in the UV spectral range below 320 nm (contribution up to 30%). For the AFDM-CCD the stray light contribution is less than 5% between 330 and 580 nm. Above 580 nm the stray light contribution slightly increases again due to the decreased sensitivity of the AFDM-CCD in this spectral range (see next subsection). In contrast, the stray light contribution of the AFDM-PDA decreases rather continuously with increasing wavelength up to a value of less than 0.1% (see Fig. 3f). However, the stray light contribution related to the lamp spectrum for the critical UV range is quite comparable for both spectroradiometers for wavelengths below 400 nm.

Field measurements were analyzed with the stray light spectra derived from the laboratory data and were compared with spectra analyzed with the stray light spectrum obtained from the atmospheric measurements. A difference of ±3% was derived mainly in the first nanometer of the actinic flux density spectrum. For wavelengths above 304 nm the difference between the I_{SL} spectra obtained in the laboratory to those from field measurements decreased to less than 1%. In addition, $J(O^1D)$ values calculated with the two stray light distributions were compared. An overall difference of less than 2% was quantified, which justifies the use of a predefined stray light spectrum from the laboratory measurements for the evaluation of field data.

2) SENSITIVITY

The sensitivity $D(\lambda)$ of the AFDM-CCD spectroradiometer (and the AFDM-PDA) is quantified by the conversion factor that transforms the measured spectral counts (I) into the actinic flux density:

$$F_a(\lambda) = \frac{I(\lambda)}{D(\lambda)}. \tag{4}$$

The procedure to determine $D(\lambda)$ is called absolute calibration where a standard irradiance lamp with known values of $F(\lambda)$ is used. For an incident angle of radiation of $\theta = 0°$, F_a and F are equivalent. The absolute calibration was performed with a standard 1000-W lamp (traceable to PTB). The standard irradiance is certified for a distance of 700 mm between the calibration lamp and the optical inlet of the spectroradiometer. To improve the calibration accuracy the procedure is carried out with two calibration distances. The first set of measurements was done at the calibration distance of 700 mm (given in the manual of the manufacturer). A second set of calibration measurements was collected at a closer distance (≈400 mm) between the lamp and the optical inlet. The latter increases the signal magnitude, which helps to improve the accuracy of the sensitivity measurement in particular in the spectral region of the CCD with low sensitivity. Each set of measurements consists of a series of lamp measurements $I_{Lamp}(\lambda)$; filter scans with a longwave pass filters of F320 and F700; and d + e measurement $I_{d+e}(\lambda)$ (with obscured optical inlet).

The stray light counts using a longwave pass filter with $\lambda_c = 320$ nm (I_{SL320}) and $\lambda_c = 700$ nm (I_{SL700}) were determined via Eq. (3). As shown above, the stray light of the CCD instrument is slightly wavelength dependent (see Fig. 3c). The stray light counts are derived from the averaged counts between 270- and 305-nm wavelength using a longwave pass filter with $\lambda_c = 320$ nm. This average serves as a reference signal to scale the filter measurement using the filter with $\lambda_c = 700$ nm, which defines the spectral shape of the stray light, with a scaling factor (s_1):

$$s_1 = \frac{\overline{I_{SL320}}^{(270–305nm)}}{\overline{I_{SL700}}^{(270–305nm)}} \quad \text{and} \tag{5}$$

$$I_{SL}(\lambda) = s_1 \times I_{SL700}(\lambda). \tag{6}$$

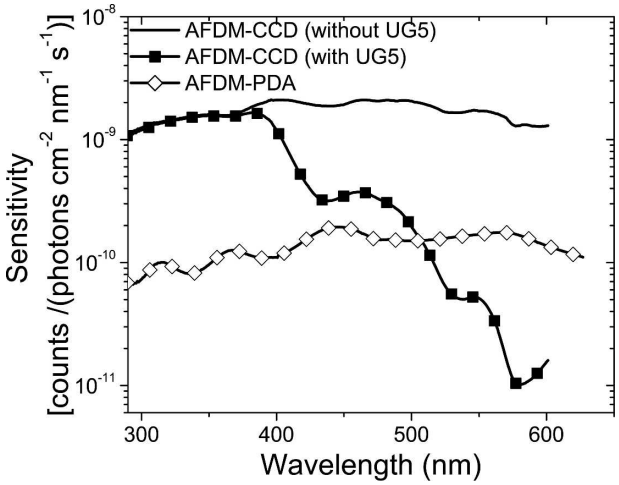

FIG. 4. Spectral sensitivity of the AFDM-PDA and the AFDM-CCD spectroradiometer.

The spectral counts calculated with

$$I(\lambda) = I_{\text{Lamp}}(\lambda) - I_{\text{d+e}}(\lambda) - I_{\text{SL}}(\lambda) \tag{7}$$

are determined for both distances. In this way a second scaling factor (s_2) is derived that links the measurements of the "near" and "far" calibrations. The factor is calculated by dividing the direct signals for each pixel. In theory the ratio should be independent of wavelength. However, due to the low sensitivity, in particular below 320 nm and above 520 nm, the measured scaling factor s_2 is noisy. Hence, the final scaling factor s_2 is determined by the ratio of the wavelength-averaged signals between 370 and 430 nm (range with lowest noise of s_2) of the near and far calibrations:

$$s_2 = \frac{\overline{I_{\text{near}}^{(370\text{–}430\text{nm})}}}{\overline{I_{\text{far}}^{(370\text{–}430\text{nm})}}}. \tag{8}$$

Now the scaling factor s_2 enables a conversion of the near signals to signals at 700-mm distance. Finally, the revised far signals are used to determine the calibration factors.

Figure 4 displays the spectral sensitivities [given in units of counts per (photons cm^{-2} s^{-1} nm^{-1})] of the AFDM-PDA spectroradiometer and the AFDM-CCD with and without using a bandpass filter (UG5, manufactured by SCHOTT AG, Mainz, Germany). Here, $D(\lambda)$ includes the sensitivity of the detector and the transmission characteristics of the optical inlet and the optical fiber. The UG5 transmission ranges from 89% at wavelengths around 350 nm to 0.7% at 580 nm. In the UV spectral range the AFDM-CCD has a sensitivity in the order of 10^{-9} counts per (photons cm^{-2} s^{-1} nm^{-1}), whereas the sensitivity of the AFDM-PDA is one order of magnitude lower [10^{-10} counts per (photons cm^{-2} s^{-1} nm^{-1})]. The spectral patterns of the AFDM-PDA and AFDM-CCD (without the UG5 filter) sensitivities are quite homogeneous over the entire spectral range. The sensitivity of the AFDM-CCD with the UG5 filter exhibits a strong wavelength dependence. This bandpass filter reduces the sensitivity mainly in the VIS spectral range by two orders of magnitude from 10^{-9} to 10^{-11} counts per (photons cm^{-2} s^{-1} nm^{-1}). In this way the bandpass filter avoids rapid saturation of the detector in the VIS range even during measurements with low integration times (20 ms). Hence, the main purpose of this UG5 bandpass filter is the adjustment of the sensitivity considering the entire wavelength range with respect to the available solar radiation. The loss of sensitivity in the VIS is negligible due to the gain of solar radiation in the VIS by five orders of magnitude compared to the UV-B. The second advantage of using the UG5 filter is the reduction of stray light by about 50%.

3) NOISE AND DETECTION LIMIT

The precision of spectroradiometer measurements is defined by the noise of the measured signals for constant measurement conditions. A quantitative measure of the noise is the signal-to-noise ratio (SNR), which is defined by

$$\text{SNR} = \frac{\bar{I}}{\text{sdv}}. \tag{9}$$

Here, $\bar{I}$ is the average of the raw counts and sdv is the standard deviation. The precision of a spectroradiometer measurement is defined as $P = 1/\text{SNR}$, where P gets smaller with an increased SNR.

Using a calibration lamp for the measurement of SNR causes additional noise due to the limited stability of the lamp output. Therefore, d + e measurements with an obscured optical inlet were performed instead of measurements with a lamp to quantify the SNR. The SNR of the AFDM-CCD was determined by the mean and standard deviation of 1000 d + e measurements using different integration times (5–400 ms). In contrast to the AFDM-PDA ($\sigma = 2$ counts), the standard deviation σ of the AFDM-CCD measurements depends on the integration time as shown in Fig. 5a. The 1000 d + e measurements for each integration time were averaged, and afterward the mean spectrum was averaged over all wavelengths. The error of the latter calculation is considered by the standard deviation. The corresponding error bars are less than the symbol size in Fig. 5a; therefore, they are not plotted in this figure. The integration time dependence of σ has an effect on the SNR, which results in a decrease of the AFDM-CCD SNR with integration time (see Fig. 5b). For typical

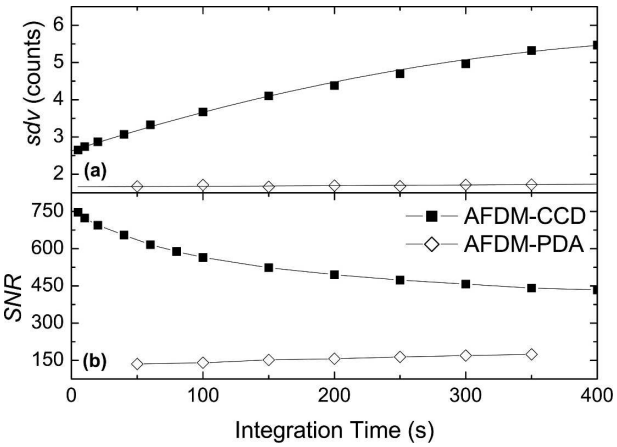

FIG. 5. (a) Standard deviation of mean signal "sdv" as a function of integration time for the AFDM-CCD and AFDM-PDA. (b) SNR dependence on the integration time for the AFDM-CCD and AFDM-PDA.

integration times between 100 and 300 ms, values of SNR between 450 and 550 are obtained. In contrast to the AFDM-CCD, the AFDM-PDA has an SNR ranging between 150 and 180 for the same integration times. Consequently, an improvement of the SNR (AFDM-CCD) in the range of a factor of 3 is obtained compared to the SNR of the AFDM-PDA.

The limit of detection, also called the noise equivalent irradiance (NEI), describes the lowest meaningful actinic flux density that can be reasonably measured. NEI is determined by the standard deviation of the d + e current σ and is calculated with

$$\mathrm{NEI}(\lambda) = \frac{\mathrm{sdv}(\lambda)}{D(\lambda)}. \quad (10)$$

NEI depends on the wavelength mainly due to the wavelength dependence of the sensitivity $D(\lambda)$. A calculation of NEI is not well defined due to the variation of σ with integration time. Therefore, NEI was determined for two assumed values of σ (three and five counts). The spectrally dependent detection limit of the AFDM-CCD with the UG5 filter ranges between 10^9 photons $\mathrm{cm}^{-2}\ \mathrm{s}^{-1}\ \mathrm{nm}^{-1}$ (UV-B) and 5–10^{11} photons $\mathrm{cm}^{-2}\ \mathrm{s}^{-1}\ \mathrm{nm}^{-1}$ (VIS). It is improved in the UV-B by one order of magnitude compared to the NEI of the AFDM-PDA system (UV-B, 10^{10} photons $\mathrm{cm}^{-2}\ \mathrm{s}^{-1}\ \mathrm{nm}^{-1}$; VIS, 3–$10^{10}$ photons $\mathrm{cm}^{-2}\ \mathrm{s}^{-1}\ \mathrm{nm}^{-1}$), which is more spectrally homogeneous.

4) EFFECTS OF SPECTRAL RESOLUTION AND FWHM

The influence of the spectral resolution and full width at half maximum (FWHM) with respect to the photolysis frequency of ozone, $J(O^1D)$, which is particularly sensitive to the spectral resolution and FWHM, was investigated using radiative transfer simulations. The calculations were performed with the "uvspec" model from the libradtran package (Mayer and Kylling 2005). Actinic flux density spectra were computed using the extraterrestrial spectrum with 0.1-nm resolution (Kurucz 1992). These spectra were adjusted to the spectral resolution of the AFDM-PDA and the AFDM-CCD (both 0.8 nm) and convoluted with different slit functions according to the FWHM of both spectrometers (AFDM-PDA, ~2.6 nm; AFDM-CCD, ~1.5 nm). Finally, $J(O^1D)$ data were derived from the adjusted actinic flux density spectra and compared to $J(O^1D)$ values derived from nonconvoluted spectra using absorption cross-section data published by Daumont et al. (1992) and quantum yields taken from Matsumi et al. (2002). An improvement of the $J(O^1D)$ accuracy in the range of 2%–4% was found for the AFDM-CCD spectroradiometer compared to the AFDM-PDA.

The impact of the spectral resolution on the accuracy of $J(O^1D)$ was also studied. As reported by Madronich and Weller (1990), the deviation between $J(O^1D)$ derived for $\Delta\lambda = 0.1$ nm and $\Delta\lambda = 0.8$ nm can get as high as 1% depending on the SZA.

TABLE 2. Estimated measurement uncertainties (in %).

Source of error	UV range ($\lambda < 400$ nm)	VIS range ($\lambda > 400$ nm)
Calibration lamp uncertainty	±5	±3
Transfer lamp uncertainty	±3	±3
Determination of receiving plane	<±1	<±1
Wavelength calibration	±5	±1
Remaining angular response error	±2	±2
d + e current offset	±5	±1
Stray light offset	±3	<±1
Total uncertainty	±10.0	±4.9

5) UNCERTAINTY ESTIMATION

The main sources of measurement uncertainties of the AFDM-CCD are quantified in Table 2. They are taken from Jäkel (2005). The largest uncertainty arises from the absolute calibration. The temporal drift of the absolute calibration and the uncertainty due to disconnection and reconnection of the optical fibers with the spectrometer are continuously observed with the transfer calibration. These transfer calibrations are performed in the laboratory and during field campaigns using different 200-W lamps. For the transfer lamps an

TABLE 3. List of instruments used during the intercomparison. Spectra between 290- and 500-nm wavelength were measured.

Acronym	Spectroradiometer type	Spectral step (nm)	FWHM (nm)	Institute
ATI	Bentham DTM 300	0.5	0.96	University of Innsbruck
GBM	Bentham DTM 300	0.5	0.64	University of Manchester
DEM	PDA	0.8	2.4	metcon
AFDM-CCD	CCD	0.8	1.5	Leibniz-Institute for Tropospheric Research

uncertainty of ±3% is estimated. The determination of the certified distance from the irradiance standard to the receiving plane of the optical inlet leads to an uncertainty of less than ±1%. In addition to the absolute calibration the spectral calibration represents the second major source of uncertainty in the UV spectral range. The manufacturer specifies an absolute wavelength accuracy of about 0.3 nm. To calculate the related uncertainty, spectra were artificially shifted by 0.3 nm. The ratio of the original spectra and the shifted spectra was calculated, and an uncertainty of ±5% in the UV range and of less than ±1% in the VIS range was observed. The error due to the nonideal angular response of the optical inlet was considered in the angular correction of the data depending on various parameters. A remaining uncertainty for that kind of correction can only be estimated (±2%). The uncertainty resulting from the signal offset components mainly affect the lowest wavelength of the measured spectra (first 3 nm). They were estimated to be ±5% for the d + e current and ±3% for the stray light contribution. These results yield a total uncertainty estimate of ±10% in the UV range and ±5% in the VIS range, calculated with Gaussian error propagation.

In terms of the $J(O^1D)$ [$J(NO_2)$] uncertainty, the stray light determination results in an uncertainty contribution of $<\pm 2\%$ [$<\pm 1\%$]. Small-scale variations of the d + e current cause an uncertainty of ±3.5% [$<\pm 1\%$]. Furthermore, the FWHM and spectral resolution contribute with $<\pm 1\%$ each. The contribution of the spectral calibration uncertainty is $<\pm 1\%$. It results in an overall $J(O^1D)$ [$J(NO_2)$] uncertainty of ±8% [±6%] including the calibration and angular response uncertainties presented in Table 2.

3. Atmospheric measurements

Examples of atmospheric measurements collected with the AFDM-CCD are presented in this section. They were performed during an international field campaign. Different approaches to removing the stray light from the measured spectrum are studied in terms of the photolysis frequency of $J(O^1D)$. Furthermore, actinic flux density and photolysis frequency measurements taken by the AFDM-CCD are compared to measurements of two double monochromators and PDA spectroradiometers.

a. Experimental

As part of the European campaign called Influence of Clouds on the Spectral Actinic Flux in the Lower Troposphere (INSPECTRO), an intercomparison of actinic flux density measurements was performed with high-precision double monochromators, PDA-based spectroradiometers from several institutes, and the AFDM-CCD. The intercomparison took place at Straubing airport, Germany (48.9°N, 12.5°W) on 6–11 May 2004. Here, measurements of two Bentham Double Triplegrating Monochromator (DTM) 300 instruments (ATI, GBM) and one photodiode array instrument (DEM) are compared to measurements of the AFDM-CCD. Table 3 gives an overview of the instruments. The Bentham instruments and DEM have been described elsewhere in more detail (Webb et al. 2002).

The intercomparison required synchronized measurements by all the scanning instruments leading to scans of 0.5-nm resolution between 290 and 500 nm with one step every 3 s. Collection of a complete spectrum took 21 min, although the Bentham DTM instruments are capable of faster scan rates. The PDA instruments and the AFDM-CCD measured actinic flux density spectra with higher time resolution. The DEM instrument yielded one spectrum within 10 s, while the AFDM-CCD measured with 200-ms integration time. To overcome the problem of the different time resolutions of the different spectroradiometers, the spectra of the AFDM-CCD were averaged over a period of 3 s according to the wavelength step width of the double monochromator. Hence, over 400 AFDM-CCD spectra were taken during 21 min. The PDA and AFDM-CCD spectra were converted to 0.5-nm-wavelength intervals by interpolation. For comparison with the scanning instruments, artificial spectra were generated for the PDA and the AFDM-CCD. For each time given for each wavelength step of the double monochromator, the matching AFDM-CCD (PDA) spectral actinic flux density was selected. This approach requires exact time

synchronization of all instruments, particularly for quickly changing atmospheric conditions.

During the intercomparison the cloud coverage of the sky was mainly more than 6 octas with intermittent periods of rain. Therefore, some uncertainties due to the insufficient time synchronization have to be considered in the data interpretation. In addition, the FWHM of all instruments differed between 0.64 and 2.5 nm, which was considered by using the SHICRIVM algorithm [software package for wavelength shift and quality control of solar spectral UV-measurements; Slaper et al. (1995)] to homogenize all spectra to an FWHM of 1 nm and correct wavelength shifts. One actinic flux density spectrum was taken each hour by the double monochromator during the intercomparison. Finally, 32 spectra taken on 5 days were used for the comparison of actinic flux density spectra and photolysis frequencies presented in section 3c.

b. Stray light effects

The influence of the stray light contribution on the photolysis frequency of ozone $J(O^1D)$ is studied for three different approaches. The first method (A) determines a wavelength-independent stray light contribution by averaging the signal offset between 270 nm and a flexible wavelength of the spectrum (the d + e current is subtracted before) where the atmospheric cutoff starts. This starting wavelength is defined by the slope of the spectrum in the spectral range of the atmospheric cutoff. The slope parameter is not a fixed value but rather a function of the magnitude of the radiation. For example, a small SZA causes a steeper slope than a large SZA. A linear function between the slope and the number of counts at a specific wavelength (here, 400 nm) was assumed. This slope function was optimized by comparing the actinic flux density spectra of the AFDM-CCD and the ATI instrument.

The second approach (B) defines a wavelength-dependent stray light signal. For that purpose the stray light measurement with a longwave pass filter with λ_c = 700 nm is used as a reference stray light spectrum. It is scaled to the stray light signal averaged between 270 and 290 nm, similar to Eq. (3). The third method (C) does not correct the stray light at all.

Figure 6 displays two time series (20 min) of $J(O^1D)$ derived from spectral actinic density measurements using these three stray light correction methods. The measurements of the spectral downwelling actinic flux densities were performed at the ground at SZA = 33° (Fig. 6a) and at SZA between 71° and 75° (Fig. 6b). Compared to SZA = 33°, much noisier $J(O^1D)$ values are noticed for large SZAs, which cannot be explained by atmospheric variations caused by clouds or aerosol particles. However, both time series show a nearly identical spectral pattern of $J(O^1D)$ derived from methods A and B, whereas method C gives an overestimation of the J values. Figures 6c and 6d display the ratios of $J(O^1D)$ derived from methods A–B and methods C–B. The deviation between the ozone photolysis frequencies by methods A and B is less than 3% for large SZAs, while for SZA = 30°, the ratio is even less than 1%. Method C overestimates $J(O^1D)$ significantly by a value of up to 15%.

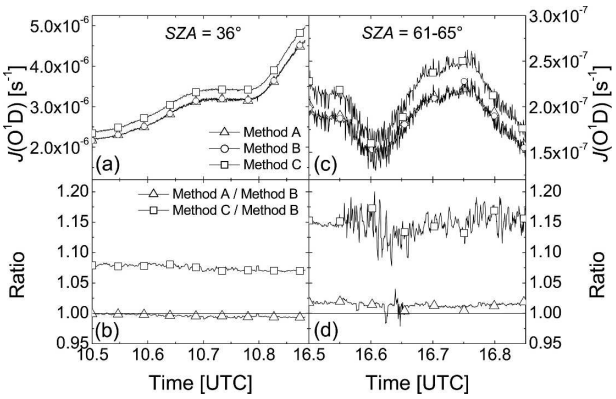

FIG. 6. Time series of $J(O^1D)$ measured with the AFDM-CCD using three methods of stray light correction for (a), (b) SZA = 33° and (c), (d) = 71°–75° for 6 May 2004, at Straubing airport in Germany. (a), (c) Method A, constant stray light contribution; method B, wavelength-dependent stray light signals; and method C, no stray light correction. (b), (d) Ratio of methods C and B as well as ratio of methods A and B. Horizontal lines in (b) and (d) represent a ratio of 1.

The methods were also tested for nitrogen dioxide (NO_2) photolysis frequencies using the absorption cross section published by Merienne et al. (1995) and the quantum yield of Troe (2000). All three methods yield nearly the same $J(NO_2)$ values (deviation less than 1%), because the contribution of the stray light to the overall signal is less than 1% above the 315-nm wavelength, and the sensitive spectral range for $J(NO_2)$ measurements is between 300 and 420 nm.

In terms of the negligible deviation between J values determined with methods A and B, it does not seem necessary to consider the stray light as wavelength dependent.

However, the comparison between the spectral actinic flux densities derived with both methods shows deviations for the first 2 nm of the spectrum (<5% for SZA = 33°, <15% for SZA = 75°). The reason of the deviation is the decrease of the spectral stray light signals up to 320 nm. The assumption of constant stray light neglects this slope. For this reason it is advisable to consider the spectral dependence of the stray light with regard to F_a, that is, to use method B.

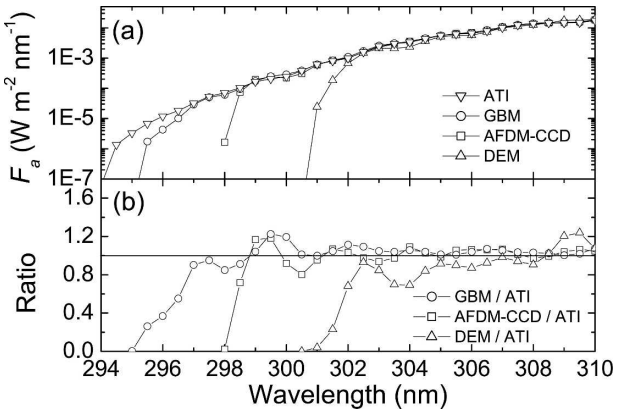

FIG. 7. (a) Spectral actinic flux density spectra measured at SZA = 33° with a PDA spectroradiometer (DEM), the AFDM-CCD, and two double-monochromator instruments (ATI, GBM) for 6 May 2004 at Straubing airport. (b) Spectral ratios of F_a of all spectroradiometers related to the ATI actinic flux density spectrum. The horizontal line marks a ratio of 1.

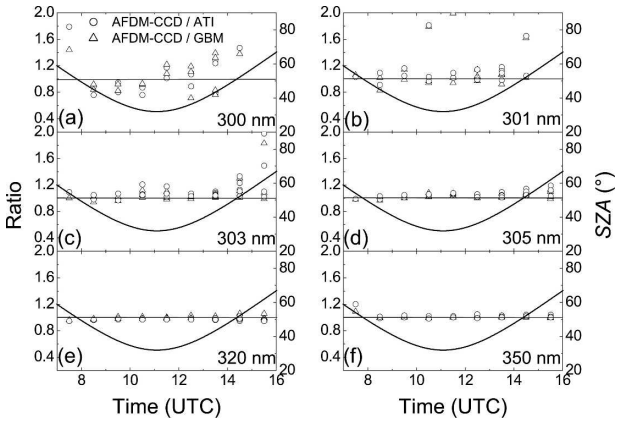

FIG. 8. (a)–(f) Ratios of double-monochromator (ATI or GBM) and AFDM-CCD measurements of the actinic flux density for 5 days displayed as a diurnal pattern: 6–11 May 2004 at Straubing airport. In addition, the SZA is plotted as a solid line. The horizontal lines represent a ratio of 1.

c. Intercomparison

1) ACTINIC FLUX DENSITIES

Figure 7a shows the artificial spectra of the PDA spectroradiometer DEM, the AFDM-CCD, as well as the ATI and GBM spectra in a logarithmic plot measured on 6 May 2004 (1030–1051 UTC) at SZA = 33°. The spectral range of between 294 and 310 nm is considered the most crucial range with regard to the sensitivity of the spectroradiometers. For wavelengths larger than 310 nm (to 500 nm), all results agree within ±10%. The double-monochromator spectra (ATI and GBM) are considered to be the measurements with the lowest uncertainty in the UV-B spectral range due to their high quality of stray light rejection. Nevertheless, the mean ratio between GBM and ATI (λ = 297–310 nm) of 1.03 ± 0.07 indicates an increased uncertainty compared to the average range of λ = 310–500 nm (GBM/ATI = 0.99 ± 0.01). The DEM spectrum starts at a larger wavelength (301 nm) compared to the double-monochromator spectra (294.5 and 295.5 nm, respectively). The AFDM-CCD spectrum shows an underestimation below 298.5 nm compared to the ATI and GBM spectra. The reason is the problematic determination of the offset. The offset represents a small difference of two signals with a high number of counts (measured signal minus d + e current) and this is highly error prone.

The spectral ratios of the actinic flux density spectra of all spectroradiometers and the ATI double monochromator for both measurements are plotted in Fig. 7b. With minor exceptions all spectra agree with the ATI data above 305 nm within ±10%. The deviations exceeding ±10% possibly originate from (i) an insufficient 0.5-nm interpolation of the spectra, (ii) uncertainties in the wavelength calibration, or (iii) an inaccurate time synchronization. Interpolation uncertainties are considered as negligible due to the fact that the GBM data are not interpolated. Nevertheless, a spectral structure of the GBM–ATI is obvious that is similar to the AFDM-CCD/ATI ratio. The uncertainty of wavelength shifts was estimated by shifting a simulated F_a spectrum by 0.2 nm. Systematic deviations of up to 10% were found, which decreased with increasing wavelength. The main effect on the spectral course of the ratios was attributed to insufficient time synchronization. This results in increasing variations between different measurements, in particular for variable cloud conditions. This fact emphasizes the need for temporal high-resolution data collection. Exemplarily, two F_a spectra taken by the AFDM-CCD within 3 s were compared. Deviations of ±20% were noticed in this short period of time.

The ratio between the double-monochromator spectra and the AFDM-CCD spectrum clearly shows the increased uncertainty of the AFDM-CCD below 300-nm wavelength (Fig. 7b). However, compared to the DEM spectroradiometer, the AFDM-CCD follows best the spectra of the double monochromators toward lower wavelengths as a result of the higher sensitivity in this spectral range.

In Fig. 8 the diurnal pattern of the ratios between the double monochromator and AFDM-CCD is depicted. For this purpose these ratios were calculated for each measurement (all in all, 32 ratios). Figure 8 shows the ratios for different wavelengths from 300 nm up to 350 nm. Additionally, the SZA is plotted. In addition to the

dependence on the SZA, the atmospheric conditions also influence the accuracy of the AFDM-CCD measurements. For large SZA and overcast conditions the intensity of the downwelling radiation is reduced and a higher sensitivity of the detector is required. The improved agreement between AFDM-CCD and the two double monochromators with increasing wavelength is obvious. Exemplarily for 300-nm wavelength, the ratio between GBM and AFDM-CCD ranges between 0.7 and 1.4, whereas for 301 nm the ratios are mostly concentrated around the ±10% range. One has to keep in mind that wavelength shifts and time synchronization problems may have an impact on these results. A closer look at Fig. 8a shows that even the differences between the two double monochromators for 300 nm can reach 10%.

2) PHOTOLYSIS FREQUENCIES

Photolysis frequencies of O_3 and NO_2 were calculated from the corrected AFDM-CCD and PDA actinic flux density spectra and from the double-monochromator spectra. For $J(NO_2)$ [$J(O^1D)$], absorption cross-section data were taken from Merienne et al. (1995) (Daumont et al. 1992), while the quantum yield data stem from Troe (2000) (Matsumi et al. 2002). The use of $J(NO_2)$ and $J(O^1D)$ investigates the AFDM-CCD's capability to determine J values in the UV-A and UV-B compared to the PDA and to the double-monochromator measurement method.

The ratios of the J values derived from AFDM-CCD/DEM/GBM measurements and the J values with respect to the ATI were calculated. A time series of the ratios for $J(O^1D)$ and $J(NO_2)$ is plotted in Fig. 9. The smallest deviations of $J(O^1D)$ values are found for the GBM (average ratio, 0.97; standard deviation, 0.19) and the AFDM-CCD data (0.99 ± 0.20). The PDA spectroradiometer underestimates $J(O^1D)$ (0.90 ± 0.20), caused by the underestimation of the UV-B radiation and the shift of the start wavelength of the DEM spectra to larger wavelengths (see Fig. 7). Figure 9b displays the ratio of the $J(NO_2)$ values. Nearly all ratios are within the ±10% range, whereby the best agreement was found for the GBM and AFDM-CCD, each with a mean ratio of 0.99 (±0.01). The ratio of the DEM spectroradiometer shows again a small underestimation compared to the ATI data (0.97 ± 0.29).

The advantage due to the high temporal resolution of the AFDM-CCD is demonstrated by comparing the derived J values with ATI results, using different scan times (ATI, 21 min per spectrum; AFDM-CCD, 200 ms per spectrum). For this comparison the J values of the AFDM-CCD were averaged over the time interval, when the ATI spectroradiometer scanned the corresponding wavelength range [for $J(O^1D)$, 290–330 nm; for $J(NO_2)$, 290–420 nm]. Table 4 summarizes the results for the measurements on 6 May 2004. The averaged values from the AFDM-CCD agree with the ATI data within ±3%. The standard deviations of the AFDM-CCD values show the variability that is missed by the low temporal resolution measurements. The variability of $J_{\text{AFDM-CCD}}$ during one ATI measurement is greater for $J(NO_2)$ (4%–24%) than for $J(O^1D)$ (2%–10%), because clouds impact upon the UV-A and VIS portions of the spectrum more than they do upon the UV-B (Seckmeyer et al. 1996; Crawford et al. 2003).

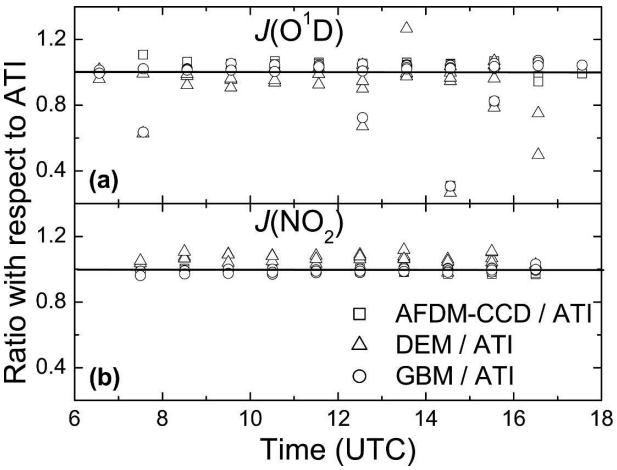

FIG. 9. (a) Ratios of $J(O^1D)$ measured with different spectroradiometers and $J(O^1D)$ derived from ATI measurements for five days: 6–11 May 2004 at Straubing airport. (b) As in (a) but for $J(NO_2)$. The horizontal lines represent a ratio of 1.

4. Summary

A spectroradiometer system equipped with a CCD detector for atmospheric measurements of the actinic flux density in the UV spectral range has been presented. This new CCD-based spectroradiometer was compared to a spectroradiometer with a PDA detector investigating several aspects, such as the sensitivity in the crucial UV-B range, the detection limit, the signal-to-noise ratio, and the determination of the offset, which includes the dark current, the electronic noise, and the stray light. A higher sensitivity (in the UV-B) of the CCD compared to PDA detector was found (one order of magnitude). The detection limit of the CCD-based instrument is improved by the same order of magnitude compared to a PDA spectroradiometer. In contrast to the PDA spectroradiometer, the CCD system is cooled by a Peltier element to reduce the signal noise and to improve the dark current and the elec-

TABLE 4. Comparison of $J(O^1D)$ and $J(NO_2)$ values derived from ATI and averaged AEDM-CCD data based on different scan times for 6 May 2004.

Start time in UTC (hhmm)	$J(NO_2)_{ATI}$ (s^{-1}) $\times 10^{-3}$	$J(NO_2)_{CCD}$ (s^{-1}) $\times 10^{-3}$	$J(O^1D)_{ATI}$ (s^{-1}) $\times 10^{-6}$	$J(O^1D)_{CCD}$ (s^{-1}) $\times 10^{-6}$
0830	2.14	2.01 ± 0.21	3.41	3.58 ± 0.37
0930	1.20	1.31 ± 0.09	2.82	2.92 ± 0.05
1030	1.47	1.47 ± 0.18	2.59	2.98 ± 0.07
1130	2.42	2.44 ± 0.40	4.69	4.93 ± 0.24
1230	1.48	1.82 ± 0.44	4.80	4.97 ± 0.54
1330	1.34	1.35 ± 0.16	1.87	1.94 ± 0.06
1430	1.85	1.75 ± 0.29	1.64	1.74 ± 0.15
1530	0.88	0.95 ± 0.37	0.83	0.87 ± 0.03

tronic offset stability. The stray light contribution of the CCD instrument, which has a magnitude similar to the PDA-based spectroradiometer, shows a wavelength dependence with a maximum near 340 nm. However, in terms of the determination of J values this wavelength dependence of the stray light of the CCD instrument can be neglected. In contrast, a wavelength-dependent and a constant stray light assumption show differences with respect to actinic flux densities mainly in the first 2 nm of the spectra. It shows that the determination of the offset is critical and requires a more thorough handling than that of the PDA spectroradiometer where the offset is nearly wavelength independent. Note that the wavelength dependence of the stray light contribution might be different for each CCD spectroradiometer. The handling gets more complicated when the stray light maximum is shifted to lower wavelengths.

An intercomparison between the AFDM-CCD and other spectroradiometer systems, which are based on single- and double-monochromator techniques, was performed with regard to actinic flux density spectra and photolysis frequencies. An improved agreement was found between the AFDM-CCD and the double monochromators compared to the agreement between single monochromators with the PDA detector. However, the increase of the sensitivity allows a determination of $J(O^1D)$. In contrast to the PDA spectroradiometer, the AFDM-CCD shows an agreement with the GBM within ±10%, independent of the intensity of the actinic flux density. Also for $J(NO_2)$, the AFDM-CCD shows an agreement with the double-monochromator systems in the range of ±5%.

Acknowledgments. The research of E. Jäkel was partly funded by the Deutsche Forschungsgemeinschaft (Contracts WE1900/6-1 and WE1900/6-2). The INSPECTRO campaign was funded by Contract EVK2-CT-2001-00130 from the European Commission. We appreciate the efforts of the project coordinator Stephan Thiel.

REFERENCES

Crawford, J., R. E. Shetter, B. Lefer, C. Cantrell, W. Junkermann, S. Madronich, and J. Calvert, 2003: Cloud impacts on UV spectral actinic flux observed during the International Photolysis Frequency Measurement and Model Intercomparison (IPMMI). *J. Geophys. Res.,* **108,** 8545, doi:10.1029/2002JD002731.

Daumont, D., J. Brion, J. Charbonnier, and J. Malicet, 1992: Ozone UV spectroscopy. I. Absorption cross-sections at room temperature. *J. Atmos. Chem.,* **15,** 145–155.

Edwards, G. D., and P. S. Monks, 2003: Performance of a single-monochromator diode array spectroradiometer for the determination of actinic flux and atmospheric photolysis frequencies. *J. Geophys. Res.,* **108,** 8546, doi:10.1029/2002JD002844.

Ehhalt, D. H., 1999: Photooxidation of trace gases in the troposphere. *Phys. Chem. Chem. Phys.,* **1,** 5401–5408.

Heard, D. E., and M. J. Pilling, 2003: Measurement of OH and HO_2 in the troposphere. *Chem. Rev.,* **103,** 5163–5198.

Hofzumahaus, A., A. Kraus, and M. Müller, 1999: Solar actinic spectroradiometry: A technique for measuring photolysis frequencies in the atmosphere. *Appl. Opt.,* **38,** 4443–4460.

Jäkel, E., 2005: An airborne system for fast measurements of upwelling and downwelling spectral actinic flux densities. Ph.D. thesis, University of Leipzig, Leipzig, Germany, 129 pp.

——, M. Wendisch, A. Kniffka, and T. Trautmann, 2005: Airborne system for fast measurements of upwelling and downwelling actinic flux densities. *Appl. Opt.,* **44,** 434–444.

——, M. Wendisch, and B. Lefer, 2006: Parameterization of ozone photolysis frequency in the lower troposphere using data from photodiode array detector measurements. *J. Atmos. Chem.,* **54,** doi:10.1007/s10874-006-9014-1.

Kurucz, R. L., 1992: Synthetic infrared spectra. *Proc. 154th Symp. of the International Astronomical Union,* Tucson, AZ, IAU, 523–531.

Lefer, B. L., S. R. Hall, L. Cinquini, R. E. Shetter, J. D. Barrick, and J. H. Crawford, 2001: Comparison of airborne NO_2 photolysis frequency measurements during PEM-Tropics B. *J. Geophys. Res.,* **106,** 32 645–32 656.

Madronich, S., 1987: Photodissociation in the atmosphere: 1. Actinic flux and the effects of ground reflections and clouds. *J. Geophys. Res.,* **92,** 9740–9752.

——, and G. Weller, 1990: Numerical integration errors in calculated tropospheric photodissociation rate coefficients. *J. Atmos. Chem.,* **10,** 289–300.

Matsumi, Y., F. J. Comes, G. Hancock, A. Hofzumahaus, A. J. Hynes, M. Kawasaki, and A. R. Ravishankara, 2002: Quan-

tum yields for production of $O(^1D)$ in the ultraviolet photolysis of ozone: Recommendations based on evaluation of laboratory data. *J. Geophys. Res.,* **107,** 4024, doi:10.1029/2001JD000510.

Mayer, B., and A. Kylling, 2005: Technical note: The libRadtran software package for radiative transfer calculations—Description and examples of use. *Atmos. Chem. Phys.,* **5,** 1975–1997.

Merienne, M. F., A. Jenouvrier, and B. Coquart, 1995: The NO_2 absorption-spectrum: 1. Absorption cross-section at ambient-temperature in the 300–500 nm region. *J. Atmos. Chem.,* **20,** 281–297.

Monks, P. S., 2005: Gas-phase radical chemistry in the troposphere. *Chem. Soc. Rev.,* **34,** 376–395.

Pilewskie, P., and Coauthors, 2003: Solar spectral radiative forcing during the Southern African Regional Science Initiative. *J. Geophys. Res.,* **108,** 8486, doi:10.1029/2002JD002411.

Seckmeyer, G., R. Erb, and A. Albold, 1996: Transmittance of a cloud is wavelength-dependent in the UV-range. *Geophys. Res. Lett.,* **23,** 2753–2755.

Shetter, R. E., and M. Müller, 1999: Photolysis frequency measurements using actinic flux spectroradiometry during PEM-Tropics mission: Instrumentation description and some results. *J. Geophys. Res.,* **104,** 5647–5661.

Slaper, H., H. A. J. M. Reinen, M. Blumthaler, M. Huber, and F. Luik, 1995: Comparing ground-level spectrally resolved solar UV measurements using various instruments: A technique resolving effects of wavelength shifts and slit width. *Geophys. Res. Lett.,* **22,** 2721–2724.

Troe, J., 2000: Are primary quantum yields of NO_2 photolysis at $\lambda \leq 398$ nm smaller than unity? *Zeit. Phys. Chem.,* **214,** 573–581.

van der Leun, J. C., X. Teng, and M. Tevini, 1998: Environmental effects of ozone depletion: 1998 assessment. *J. Photochem. Photobiol.,* **46B,** 1–108.

Webb, A. R., et al., 2002: Measuring spectral actinic flux and irradiance: Experimental results from the Actinic Flux Determination from Measurements of Irradiance (ADMIRA) project. *J. Atmos. Oceanic Technol.,* **19,** 1049–1062.

Wendisch, M., D. Müller, D. Schell, and J. Heintzenberg, 2001: An airborne spectral albedometer with active horizontal stabilization. *J. Atmos. Oceanic Technol.,* **18,** 1856–1866.

——, and Coauthors, 2004: Airborne measurements of areal spectral surface albedo over different sea and land surfaces. *J. Geophys. Res.,* **109,** D08203, doi:10.1029/2003JD004392.

——, and Coauthors, 2005: Impact of cirrus crystal shape on solar spectral irradiance: A case study for subtropical cirrus. *J. Geophys. Res.,* **110,** D03202, doi:10.1029/2004JD005294.